AMORPHOUS PHASE FORMATION ANALYSIS OF RAPIDLY SOLIDIFIED CoCr DROPLETS

A-A Bogno[1], C.Riveros[1], D.Li[2], H. Henein[1]

[1]Department of Chemical and Materials Engineering University of Alberta
Edmonton, AB, Canada

[2]CanmetMATERIALS, Natural Resources Canada
Hamilton, ON, Canada

ABSTRACT

This paper investigates amorphous phase formation and rapid solidification characteristics of a CoCr alloy. High cooling rate and high undercooling-induced rapid solidification of the alloy was achieved by impulse atomization in helium atmosphere. Two atomization experiments were carried out to generate powders of a wide size range from liquid CoCr at two different temperatures. Amorphous fraction and kinetic crystallization properties of impulse atomized powders were systematically quantified by means of differential scanning calorimetry. In addition, different but complementary characterization tools were used to analyze the powders microstructures. The fraction of amorphous phase within the investigated powders is found to be promoted by high cooling rate or smaller powder size. The critical cooling rate for amorphous phase formation, which is influenced by the oxygen content in the melt, is found to be ~3×10^4 Ks^{-1} and corresponds to a 160-µm-diameter powder atomized in helium. Hardness of the powders is found to follow a trend that is described by the Hall–Petch relation when a relatively high fraction of crystalline structures is present and decreases with the fraction of amorphous phase.

Key words: Atomization, Rapid Solidification, Co-based alloys , Metallic glasses, Crystallinity, bulk metallic glasses, Calorimetry, Enthalpy, High entropy alloys , x-ray diffraction, microscopy, Microhardness, Hall-Petch

1. INTRODUCTION

Metallic glasses have many attractive intrinsic properties, for example, strength, corrosion resistance, soft magnetism, and high moldability in the supercooled region, because the atoms are disordered and there is no long-range periodicity. In general, glassy alloys combine both high elasticity and high strength. The very first amorphous alloy was discovered when a splat quenching induced rapid solidification of small amounts of $Au_{75}Si_{25}$ (Au-25at%Si) yielded an amorphous alloy [1]. Since this discovery, there has been an unprecedented interest in amorphous alloys among metallurgists and material scientists around the world that led to the development of numerous production methods [2,3]. The new materials named *metallic glasses* have remarkable properties including strength and corrosion resistance. However, the first generation of metallic glasses has some drawbacks that include the necessity of very high cooling rates (~10^5 k/s) limiting the production of these materials to thin foils (1-100µm). A remarkable progress in the development of these newly found materials was made with the reported preparation of a 10 mm diameter ingot of a fluxed $Pd_{40}Ni_{40}P_{20}$ glass[3]. They discovered that the cooling rate could be highly reduced simultaneously with the increase of thickness of the metallic glass. Later on, Inoue and co-workers [4] reached an optimal metallic glass diameter of 72 mm by adding Cu to Pb-Ni-P alloy and varying the Ni and Cu concentrations. Metallic glasses with ingot diameters > 1 mm are called *Bulk metallic Glasses* (BMGs). BMGs have a high potential as advanced engineered materials due to their strength and corrosion resistance properties and therefore represent a very dynamic research field in material science with wide application. Several hundreds of different BMG materials are known and commercially manufactured nowadays. Their production methods include centrifugal casting [5] or water quenching [6]. A key requirement for a BMG is that the material shall have a high glass forming ability (GFA). BMGs form in a variety of systems including Fe-and Co-based alloys [7, 8]. Typically, these systems contain three to five constituents, with a large atomic size mismatch, a negative enthalpy of mixing among the main three elements and a composition close to a deep eutectic. The eutectic temperature of a BMG is significantly lower than the melting point of its individual constituents, which makes it easier to quench it into a glassy state. In addition the alloy needs to be cooled from its liquid state with a

very large undercooling of the melt. The degree of undercooling is influenced by several factors including: The initial liquid viscosity, the rate of increase of viscosity during cooling, the interfacial energy between the melt and crystal, the temperature dependence of solid-liquid interface free energy, the imposed cooling rate and the efficiency of heterogeneous nucleating agents. Provided an appropriate alloy composition, glassy materials can be obtained at high cooling rate as well as at low cooling rate (BMGs). Thermal stability of metallic glasses is influenced by two main factors: the activation energy E_a and the supercooled liquid region ($\Delta T_x = T_X - T_g$) where T_x and T_g are the crystallization and the glass transition temperatures respectively. A glass is said to be more thermally stable than the other when these two factors are relatively higher.

CoCr alloys are cladding materials generally used for hardfacing applications. Due to their high alloy content they cannot be produced by conventional forming techniques in the form of wire or sheet. Their production form is therefore limited to powders and rods. In its 2014 edition, Wohlers reported the use of CoCr alloy in powder bed Additive Manufacturing (AM); this makes the production and analysis of CoCr powder more interesting. The objective of the present work is to evaluate the glass formability (critical cooling rate) and mechanical properties of industrial CoCr alloy (Stellite®) in the form of powders generated by two containerless techniques: The Impulse Atomization (IA)[9] and the gas atomization (GA)[10]. High undercooling and high cooling rate induced containerless techniques is expected to offer the possibility to achieve amorphous solidification of such a high-alloy material.

2. POWDERS PRODUCTION

Throughout this manuscript, a liquid droplet that has completely solidified will be referred to as powder, while a droplet will refer to a spherical molten material. In this work, two types of powders are investigated. The first type, provided by Kennametal Inc., is produced by gas atomization and is referred to as GA powders. The GA powders are one of commercial Stellite_ CoCr alloys, SF12. The main chemical composition is shown in Table I.

The second category of powders, referred to as IA powders, was produced by IA at the Advanced Materials Processing Laboratory (AMPL) at the University of Alberta. Two IA runs namely run #1 and run #2 were carried out to produce powders. Charge materials for IA in run #1 consisted of GA Stellite® alloy SF12 powders, while in run #2 the charge materials of the same composition consisted of small ingots of approximately 10 mm diameter. Oxygen content has been analyzed on the charge materials before atomization: The ingots are found to contain 0.0085 pct oxygen and the GA Stellite® alloy SF12 powders contained 0.034 pct oxygen that is an order of magnitude higher than the ingots oxygen content. Both IA runs consisted in heating the charge materials by induction to 1773 K and 1673 K (1400 °C and 1500 °C), respectively, for run #1 and run #2 inside a fully dense alumina crucible and then atomizing the melt into droplets that solidify rapidly by losing heat to a stagnant helium atmosphere containing less than 30 ppm oxygen. After atomization, the rapidly solidified droplets (powders) were collected in a beaker; sieve analysis was then carried out using a sieve set accordingly with the metal powder industries federation (MIPF) Standard 05 (Standard Test Method for Sieve Analysis of Metal Powders, American Society for Testing and Materials (ASTM) B214, 2011). Sieves with the aperture from 1.4 mm to less than 125 µm were used and the powders were thus separated into different size ranges varying from 125 to 1180 µm.

A log-normal size distribution of the IA powders from run #1 is plotted (Figure 1(a)) and compared with the log-normal size distribution of the reference GA powders (Figure 1(b)). While the reference powder size distribution yielded a D50 (mass median powder size) as small as 6.95 µm compared to 586 µm for IA powders, the standard deviation of the latter is only 1.5 as compared to 2.3 for the GA reference powders, proving the potential of narrow-size distribution of powders generated by IA (similar results are obtained with IA powders from run #2).

3. POWDERS COOLING RATES ESTIMATION

Liquid cooling rate prior to any phase transformation within the IA droplets is an important parameter that influences amorphous formation. It depends on the atomization atmosphere and is difficult to measure during IA experiments. Therefore a solidification model of atomization[11] has been used to estimate the cooling rate of each investigated droplet. The

model which is based on the quantification of heat exchange between a droplet and the surrounding gas in an environment with high temperature gradient has been developed from Wiskel's heat transfer model formulation[12,13] and validated[11,14]. It assumes a uniform temperature within the entire falling droplet. Cooling rate is controlled by the heat exchange between the stagnant gas and the atomized droplets and therefore depends upon not only on the material properties but also on the nature of the gas in the atomization chamber (helium in this case) and the droplets initial falling velocity and size. For the majority of IA metallic alloys of droplets size ranging from 100 μm to 1000 μm, the value of $0.5ms^{-1}$ is found to be the initial velocity [11] . The size of a droplet in the present study is defined as the average value of each investigated size range. Cooling starts at the atomization temperature and continues by heat loss to the quiescent atmosphere during its fall (Figure 2). Heat loss to the gas, mainly through convection, is a result of the relative velocity between the powder and the atomization gas. Indeed, it has been shown that radiation heat loss has a small effect (around 3.5% of the total heat loss) therefore considered negligible[11].

Material properties of the investigated alloy used in the simulations and the method used to obtain the values are summarized in Tables 2. The initial temperatures of the droplets are 1500°C and 1400°C respectively for run#1 and run#2.

In table 2 "ideal Solution" method consists in multiplying the sum of parameters of each individual element by the mass percent of the alloy, while DSC and Thermo-Calc methods simply refer to parameters obtained by means of DSC and Thermo-Calc software respectively.

After running the model with parameters corresponding to the investigated alloy, cooling rates are deduced from the slopes of each generated cooling curve (Figure 3a). Figure 3b shows that the estimated cooling rates are consistent for both run#1 and run#2, thus melt superheat (100°C) effect on cooling rate is negligible.

4. MICROSTRUCTURAL ANALYSIS OF THE POWDERS

4.1. Phase identification

In order to evaluate the crystallinity and identify the phases present in the microstructures of the produced powders, XRD was carried out on the IA powders as well

as the GA powders (powder size <20 µm and 20-25µm). A cobalt target was used and the working voltage and current were respectively 38KV and 38mA. The 2θ scanning range was 5-90 degrees, the scan rate was 2 degrees per minute and the sampling width was 0.02 degrees. Based on previous results obtained from IA of $\{(Fe_{60}Co_{40})_{75}B_{20}Si_5\}_{96}Nb_4$ powders [15], for the present investigation powders within the following size ranges were selected from run#1: <180µm, 180-212 µm, 212-250 µm, and 250-300 µm. And the following size ranges were selected from run#2: <125 µm, 125-150 µm, 150-180 µm, 180-212 µm, 212-250 µm, 250-300 µm, 300-355 µm, 355-425 µm. Analysis of the diffraction patterns was carried out using the commercial software MDI's JADE+ ICDD Database.

Figure 4 shows a comparison of XRD patterns corresponding to investigated powders from run#1(Figure 4a) and run#2 (Figure 4b) and the GA reference powders (Figure 4a). Diffraction patterns of the GA reference powders (size less than 20µm) show a relatively broad and shallow peak, characteristic of amorphous phases. Crystalline peaks are observed on all the diffraction patterns of IA powders in run#1, which means that none of the investigated IA powders from that run are fully amorphous. However, it can be said that powders with size <180µm and between 180-212 µm contain a significant fraction of amorphous phase since a relatively broad and shallow peak is observed on their diffraction patterns.

Figure 4b shows a comparison of XRD patterns corresponding to the investigated powders obtained in run#2. The broad and shallow amorphous peak characterizing amorphous phases is observed on the diffraction patterns of powder size range starting from 212-250 µm going down.

Three crystalline peaks are observed in all the investigated non-fully amorphous powders. These correspond to fcc-Co and the protruding peak from the shallow amorphous pattern of the GA powders with size ranging from 20-25 µm corresponds to Co (Ni, Fe), which is an austenitic fcc-Co phase. These XRD results suggest that Run#2 (atomization from re-melted ingots) yields higher critical powder size (212-250 µm) for amorphous formation than run#1 (atomized re-melted GA-powders) in which fully amorphous powders were not achieved even at sizes <180µm. This could be attributed to the melt in

run#1 having more oxygen content as the charge materials consisted of remelted GA powders.

4.2. Metallography

Investigated powders in each size range were cold mounted in epoxy resin and ground using abrasive sand papers of different grit numbers, from a coarser 320 all the way to a finer 1200. Then the samples were polished using a polycrystalline diamond suspension starting with a diamond size of 9 µm to a fine 1 µm. The grinding and polishing were performed with a Buehler EcoMet 250 automatic grinder polisher. The samples were then etched using Marble's reagent consisting of 10 grams $CuSO_4$, 50mL HCl, 50mL distilled water, and 2-3 drops of H_2SO_4.

Figure 5 shows optical micrographs of the investigated IA powders. While Figure 5a shows no visible evidence of crystal structure within the powders of size range 212-250 µm, Figure 5b shows a mixture of crystalline and amorphous phase. Figure 5c shows a fully crystalline structure with large powders of size range 355-425 µm. As the powder size increases, the fraction of amorphous phases decreases while the fraction of crystalline precipitates increases.

4.3. Estimation of Amorphous Fractions

As previously described by Ciftci *et al* [15] calorimetry analysis can be used to study the recrystallization behaviors of amorphous powders and also to estimate the amorphous fraction within a given powder microstructure. This is achieved by the measurement of enthalpy of recrystallization. This enthalpy corresponds to the area under the first peak of a DSC heating curve as shown in Figure 6.

Amorphous fraction ($A_{\%}$) of each IA powder (IA) is calculated following Equation (1).The amorphous fraction of the reference GA powders (Ref) is considered to be 100%.

$$A_{\%} = 100 \times \frac{\Delta H_k(IA)}{\Delta H_k(Ref)} \quad (1)$$

Figure 7 shows the variation of $A_{\%}$ with powder size range and cooling rate. As expected *A%* increases with decreasing powder size (Figure 7a) and therefore with increasing cooling rate (Figure 7a'). Indeed cooling rate, a parameter that also depends on

the cooling gas, increases with decreasing powder size [13]. For each powders size range, the cooling rate of the average droplet size was estimated using a solidification model of atomized droplets which is described in [11]. By extrapolating the results of the amorphous percentage as a function of average powder size and cooling rate in run#1, it can be anticipated that a 100% amorphous powder may be obtained at a cooling rate of about 3×10^4 Ks^{-1} corresponding to an average IA powder size of 160µm. However, from run#2 the powder size corresponding to that cooling rate yields 99% amorphous phase which is almost the anticipated 100%.

5. THERMAL ANALYSIS OF THE GLASSY CoCr POWDERS

5.1. Thermal Stability

Thermal stability of an amorphous alloy can be evaluated based on the width of the supercooled liquid region (SLR), and the recrystallization activation energy. The SLR which is the difference between the glass transition temperature and the recrystallization temperature is given by a DSC heating curve of the investigated sample. The larger the SLR (higher recrystallization activation energy) is, the more stable the amorphous alloy is said to be. High recrystallization activation energy is important because it means that more energy is required for the recrystallization process to occur. DSC experiments were carried out at CanmetMaterials. 500 mg of IA-powders as well as fully amorphous GA reference powders (Stellite SF12 of size range <20µm) were heated at three different speeds β (5, 10, 15 $Kmin^{-}1$) from room temperature to 1470K under argon atmosphere.

Figure 8 shows the heating curves obtained by DSC analysis of the GA reference powders at three different heating rates. The characteristic temperatures corresponding to each heating rate are identified. These include the glass transition temperature, T_g (the point of inflection), followed by T_x, the temperature at which recrystallization starts and T_p the peak temperature of the first crystallization event. With these known temperatures, the width of the SLR ($\Delta T_x = T_x - T_g$) for each heating rate could be calculated and the results are summarized in Table 3.

The activation energy Ea, required for crystallization was then determined according to two different models derived from the Arrhenius equation and based on non-

isothermal kinetics: The *Ozawa model* and *the Kissinger model* described in[16]. These models yield activation energies following Equations (1) and (2) respectively.

$$\ln(\beta) = -\frac{E_a}{R}\left(\frac{1}{T_p}\right) + \ln\left(\frac{AE_a}{R}\right) \quad (1)$$

$$\ln\left(\frac{\beta}{{T_p}^2}\right) = -\frac{E_a}{R}\left(\frac{1}{T_p}\right) + \ln\left(\frac{AR}{E_a}\right) \quad (2)$$

Where, R is the gas constant, and A is the frequency factor. The activation energy Ea could be deduced from the plots shown in Figure 9a&9b of $ln\left(\frac{\beta}{{T_p}^2}\right)$ *Vs* $\frac{1000}{T_p}$ and $\ln(\beta)$ *Vs* $\frac{1000}{T_p}$ respectively following equations (1) and (2).

The characteristic temperatures *Tp*, *Tg* and the corresponding Ea are summarized in Table 4.

As can be noted, the variation of Ea obtained from the two models is as negligible as 4.6%. This sort of variation has previously been observed in similar results conducted on different BMGs [15–19].

In Figure 10, a comparison of Ea of the investigated CoCr-base metallic glass powders with reported Ea from different BMGs[15–19] shows that the investigated powder is not the most thermally stable metallic glass but still remains as stable as FeSi-and CuZr-BMGs. However, FeCo-base metallic glass powders ($\{(Fe_{60}Co_{40})_{75}B_{20}Si_5\}_{96}Nb_4$ are found to be the most thermally stable among the Ea found in the literature.

6. MECHANICAL PROPERTIES MEASUREMENT

Vickers Microhardness tests were performed on the investigated IA powders using a Wilson VH3100 automatic Vickers hardness tester. After etching with Marble's reagent the ground and polished powders, two indentations were randomly applied over the surface of each powder using a 200gf test force for a holding time of 5 sec. A total of 20 indentations were thus obtained for each range of IA powder size.

Figure 11 shows the variation of average vickers micro-hardness with average powder size from both run#1 and run#2. As can be seen, in both cases, hardness increases with powder

size from a value of ~1100Hv corresponding to the hardness of a 100% amorphous powder before reaching a maximum value (1200 Hv and 1400 Hv for run#1 and run#2 respectively) at average powder size of 250μm (run#1) and 350μm (run#2). Then hardness decreases from to a minimum value of less than 1000 Hv.

The (same) trend observed in both cases is similar to the Hall-petch grain boundary strengthening relation (from coarser to finer powders) followed by negative (inverse Hall-petch) behaviour of the material when crystallite / powder size reaches a certain minimum value[20–23].

The Hall-Petch relation states that the yield strength (or hardness) increases monotonically with decreasing average grain size *d* according to equation (3).

(

$$\sigma = \sigma_0 + k.d^{-0.5} \qquad (3)$$

where σ_0 is the friction stress, *k* a material dependent constant and *d* the grain size.

Assuming that in our case *d* is proportional to the powder size, hardness can be plotted as a function of the inverse square root of the average powder size that we also call *d* as shown in Figure 12.

It can be seen from Figure 12a that hardness variation in run #1 follows the Hall-Petch trend. However, hardness variation with the inverse square root of the average powder size in run#2 does not follow the same trend. This variation of hardness not following the Hall-Petch trend in run#2 can be attributed the refinement of grains below a critical value[24] in run#2 due to the relatively higher undercoolings (characterized by higher amorphous fractions) experienced by the droplets in that run. However, it is not very clear why run#2 shows such a high maximum hardness value of 1400Hv. This value is likely due to precipitation of more carbides and borides in run#2. Co-based superalloys are known to be very hard alloys due to the precipitations of metal carbides and metal borides[25]. In run#1 because of the presence of more oxygen, precipitations of such hardening phases might have been altered. It is worth noting that the overall micro-hardness is higher at higher amorphous fractions (or smaller powder size *d*).

7. CONCLUSIONS

Rapid solidification of CoCr alloy was achieved by Impulse Atomization under helium atmosphere. Using Gas Atomized commercial Stellite® SF12 CoCr-based alloy powders as reference, calorimetry analysis was carried out to estimate the amorphous fraction from the percentage of crystallinity in the investigated impulse atomized powders as a function of their sizes / the cooling rate. As expected, amorphous fraction is promoted by high cooling rate and smaller droplet size. The critical cooling rate for amorphous phase formation in powders produced by Impulse Atomization is found to be ~3×10^4 Ks^{-1} and corresponds to an average IA powder size of 160µm atomized in helium. Hardness variation in CoCr powders is found to follow the Hall-Petch trend. In this work, calorimetry has proven to be an efficient technique in determining the amorphous fractions; however, more accurate results could have been obtained by means of Neutrons Diffraction (ND) analysis technique. One of our submitted works for publication shows that ND yields a higher fraction of amorphous phase as compared to the calorimetry technique, probably because a much larger mass of powders is used for ND analysis.

AKNOWLEDGEMENT

The authors are grateful to the Natural Sciences and Engineering Research Council of Canada (NSERC), KENNAMETAL Inc. for financial support and CanmetMaterials for providing DSC analysis.

References

(1) KLEMENT, W.; WILLENS, R. H.; DUWEZ, P. *Nature*. 1960, pp 869–870.

(2) Chen, H. S.; D.Turnbull. *Appl. Phys. Lett.* **1967**, *10* (10), 284.

(3) H.-W. Kui, A.L. Greer, and D. T. *Appl. Phys. Lett.* **1993**, *63*, 2342.

(4) A.Inoue, N Nishiyama, and H.M, K. *Mater. Trans. JIM* **1997**, *38*, 179.

(5) Q. S. Zhang, , D. Y. Guo, A. M. Wang, H. F. Zhang, B. Z. D. and Z. Q. H. *Intermetallics* **2002**, *10*, 1197–1201.

(6) Y. Zhang, D. Q. Zhao, R. J. W. and W. H. W. *Acta Mater.* **2003**, *51*, 1971–1979.

(7) Suryanarayana, C.; Inoue, A. *Int. Mater. Rev.* **2013**, *58* (3), 131–166.

(8) Inoue, A.; Shen, B. L.; Chang, C. T. *Intermetallics* **2006**, *14* (8-9), 936–944.

(9) Henein, H. *Mater. Sci. Eng. A* **2002**, *326* (1), 92–100.

(10) Mullis, A. M.; Bigg, T. D.; Adkins, N. J. *J. Alloys Compd.* **2015**, *648*, 139–148.

(11) Prasad, A.; Mosbah, S.; Henein, H.; Gandin, C.-A. *ISIJ International*. 2009, pp 992–999.

(12) Wiskel, J. B.; Henein, H.; Maire, E. *Can. Metall. Q.* **2002**, *41* (1), 97–110.

(13) Wiskel, J. B.; Navel, K.; Henein, H.; Maire, E. In *Canadian Metallurgical Quarterly*; 2002; Vol. 41, pp 193–204.

(14) Gandin, C.-A.; Mosbah, S.; Volkmann, T.; Herlach, D. M. *Acta Mater.* **2008**, *56* (13), 3023–3035.

(15) Ciftci, N. Ellendt, N.Von Bargen, R.Henein, H. Mädler, L.Uhlenwinkel, V. *J. Non. Cryst. Solids* **2014**, *394-395*, 36–42.

(16) Minić, D., Gavrilović, A., Angerer, P., Minić, D., & Maričić, A. *J. Alloys Compd.* **2009**, *482*, 502–507.

(17) Fraczyk, A. *Techn. Sc* **2011**, *1*.

(18) Lee, K. S., & Lee, Y. S. *2012* **2012**, *5*, 2472–2478.

(19) Wang, H., Gao, Y., Ye, Y., Min, G., Chen, Y., & Teng, X. *J. Alloys Compd.* **2003**, *353*, 200–206.

(20) Hansen, N. *Scr. Mater.* **2004**, *51* (8 SPEC. ISS.), 801–806.

(21) Meyers, M. A.; Mishra, A.; Benson, D. J. *Prog. Mater. Sci.* **2006**, *51* (4), 427–556.

(22) Takeuchi, S. *Scr. Mater.* **2001**, *44* (8-9), 1483–1487.

(23) Saada, G. *Mater. Sci. Eng. A* **2005**, *400-401* (1-2 SUPPL.), 146–149.

(24) Scattergood, R. O.; Koch, C. C. *Scr. Metall. Mater.* **1992**, *27* (9), 1195–1200.

(25) Gholipour, A.; Shamanian, M.; Ashrafizadeh, F. *J. Alloys Compd.* **2011**, *509* (14), 4905–4909.

(26) Trexler, M. M.; Thadhani, N. N. *Prog. Mater. Sci.* **2010**, *55* (8), 759–839.

List of tables

Table 1 Nominal composition of Stellite® alloy SF12 (as reported on MatWeb database)

Element	Co	Cr	Ni	W	Si	Fe	B	C
Wt%	Bal.	19	14	9	3	3	2.5	0.9

Table 2 Material Properties Used in the Simulations and the Method Used to Obtain the Values

Material properties / boundary condition	CoCr alloy	Method
Liquid density [$kg.m^{-3}$]	8558	Ideal Solution
Thermal Conductivity [$W.(mK)^{-1}$]	107	Ideal Solution
Liquidus [K]	1373	DSC
Latent Heat [$J.kg^{-1}$]	$4.11.10^5$	Ideal Solution
Density at RT [$kg.m^{-3}$]	9069	Ideal Solution
Cpl [$J.(kgK)^{-1}$]	759	*Themo-Calc® Software
Cps [$J.(kgK)^{-1}$]	820	Themo-Calc Software
Stagnant gas temperature [K]	303	Thermocouple measurement

**Thermo-Calc, Version 1.1, 2008; Database SSOL4 (Alloy Solutions Database v4.9f).*

Table 3: Characteristic temperatures of glassy CoCr alloys at different heating rates

β (kmin^{-1})	T_g(K)	T_x(K)	ΔT_x(K)
5	710	736	26
10	747	756	9.6
15	750	760	9.3

Table 4: Activation energy, Ea using Kissinger and Ozawa model and error between the two models

β(k.min^{-1})	5	10	15
Tp [k(°C)]	788 (515)	802 (529)	808 (535)
Ea- Kissinger model (kJ.mol^{-1})		272	
Ea -Ozawa model (kJ.mol^{-1})		285	
Ea variation usng Kissinger and Ozawa model (%)		4.6	

List of figures

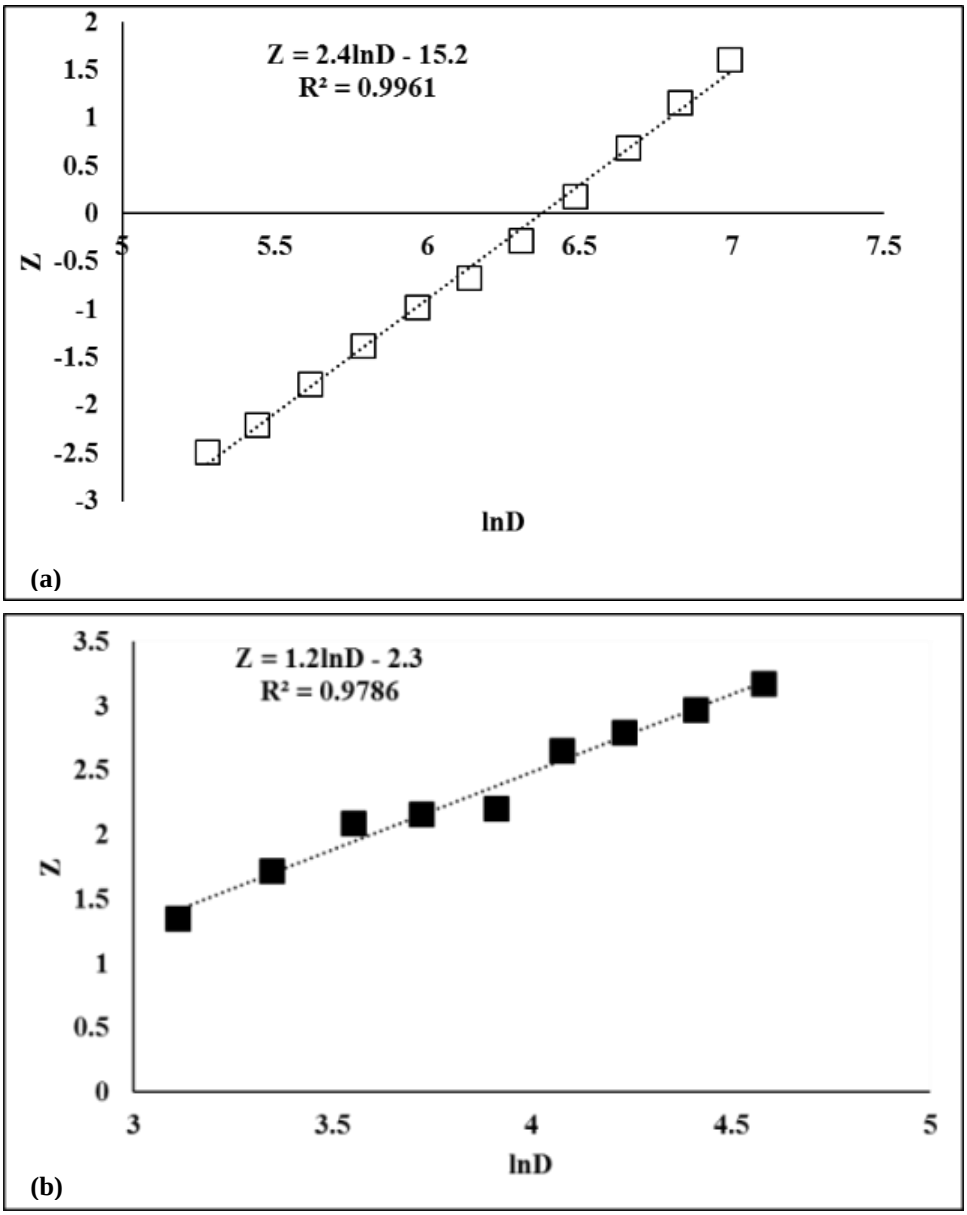

Figure 1*: Log-normal size distribution of the (a) IA droplets from run#1 and (b) GA reference powders, D is the average size (diameter) in µm and Z is the probability*

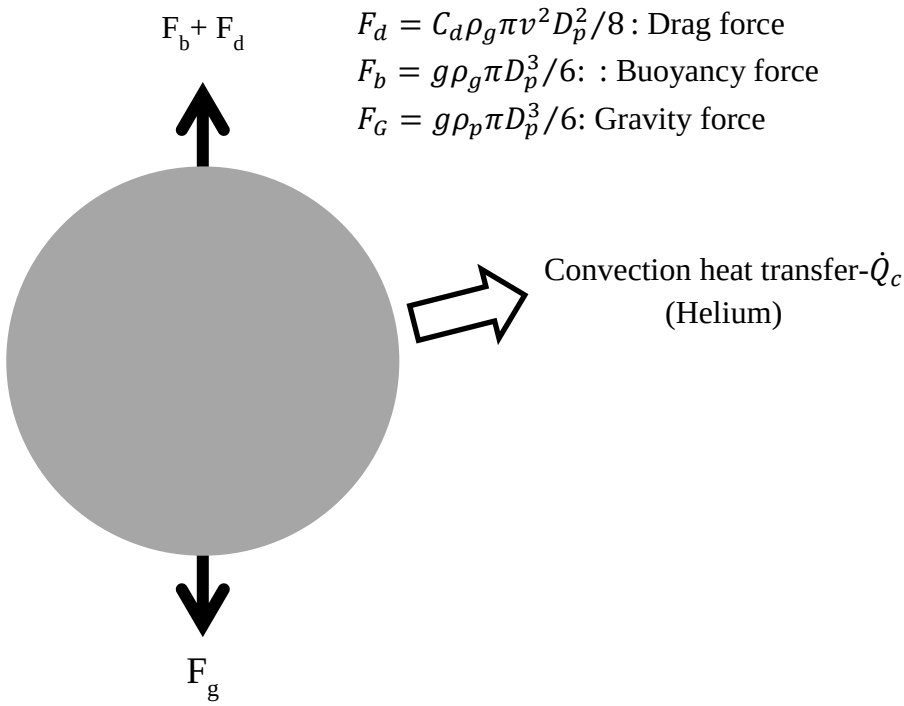

Figure 2: *Schematic of a falling liquid droplet during IA*

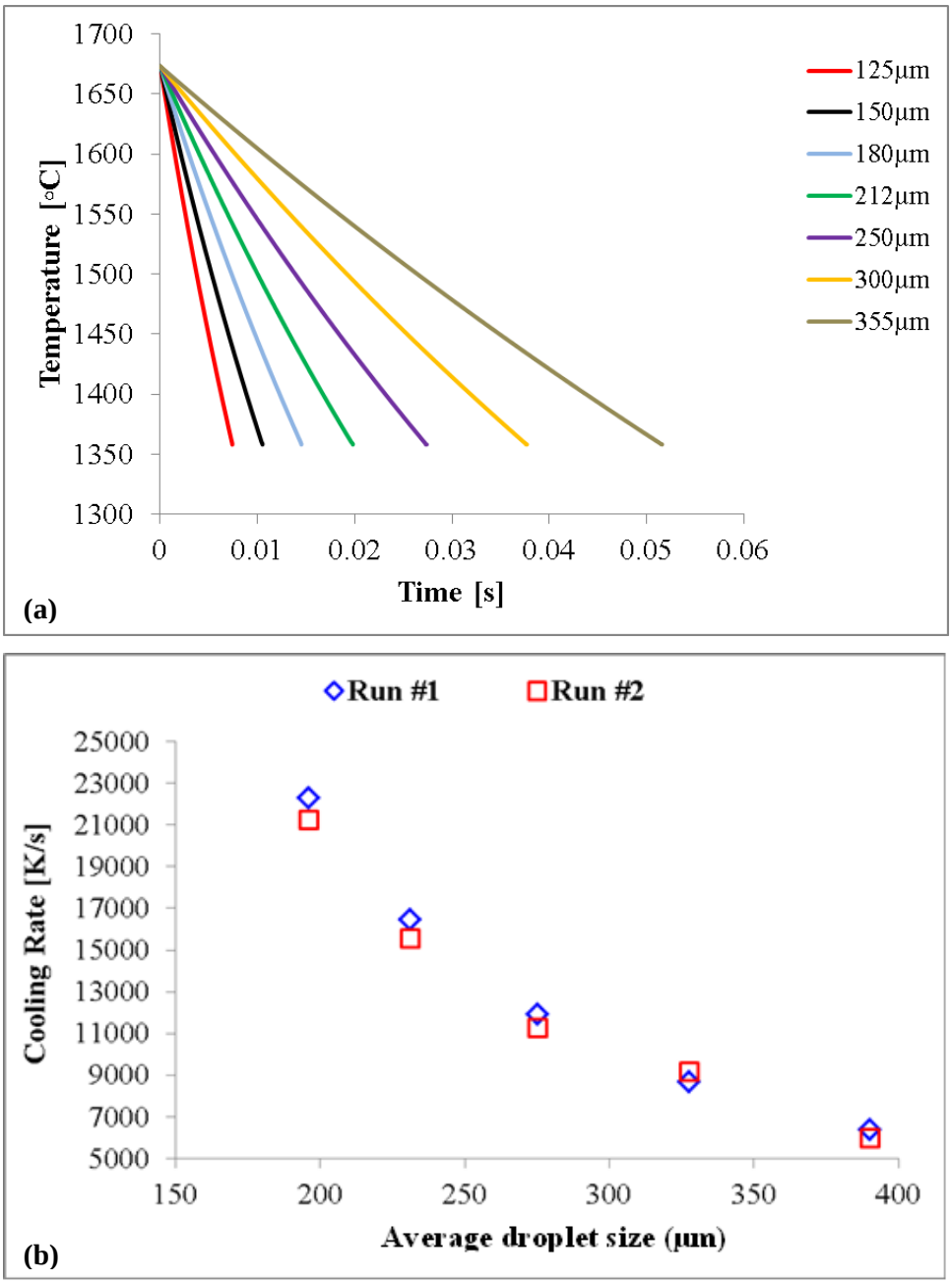

Figure 3: *(a) Thermal model[11] calculations of cooling curves of CoCr droplets of different sizes obtained in run#2 (b) variation of liquid cooling rate with average droplet size.*

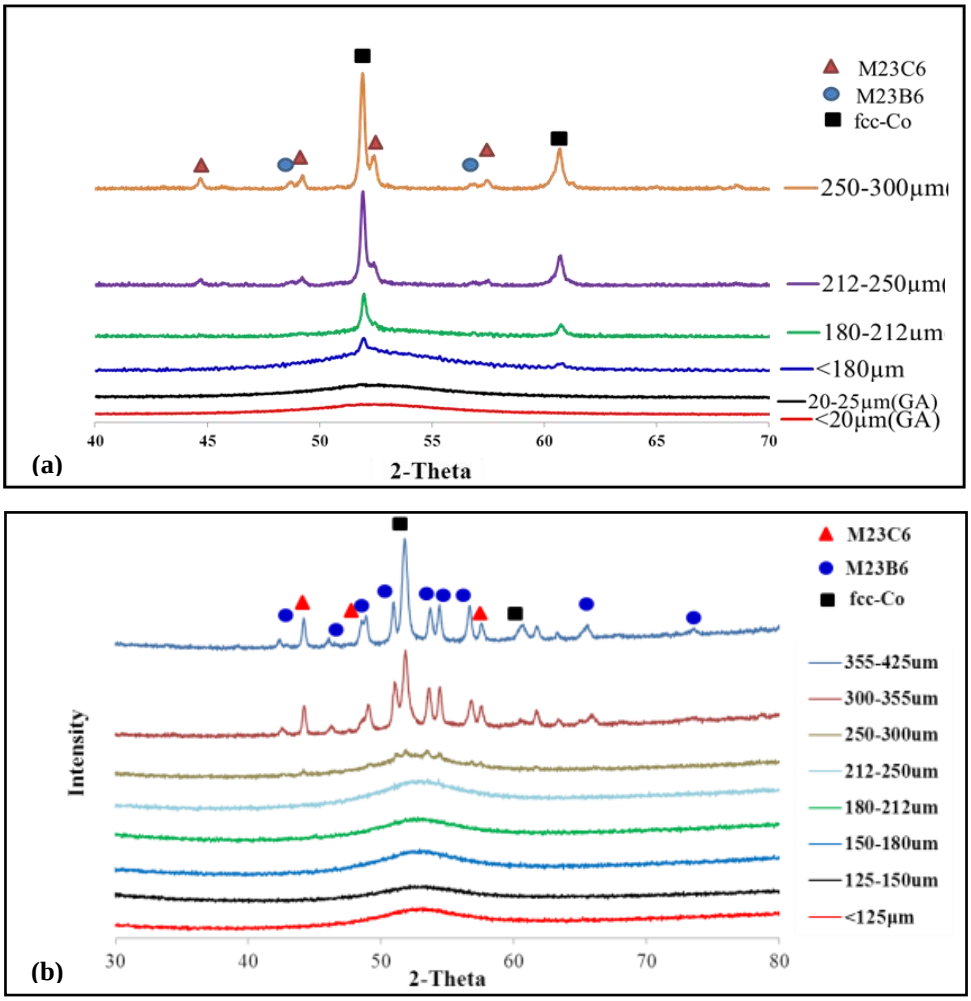

Figure 4*: XRD patterns for powders of different size ranges obtained by IA and GA (a) Run#1 (b) run#2*

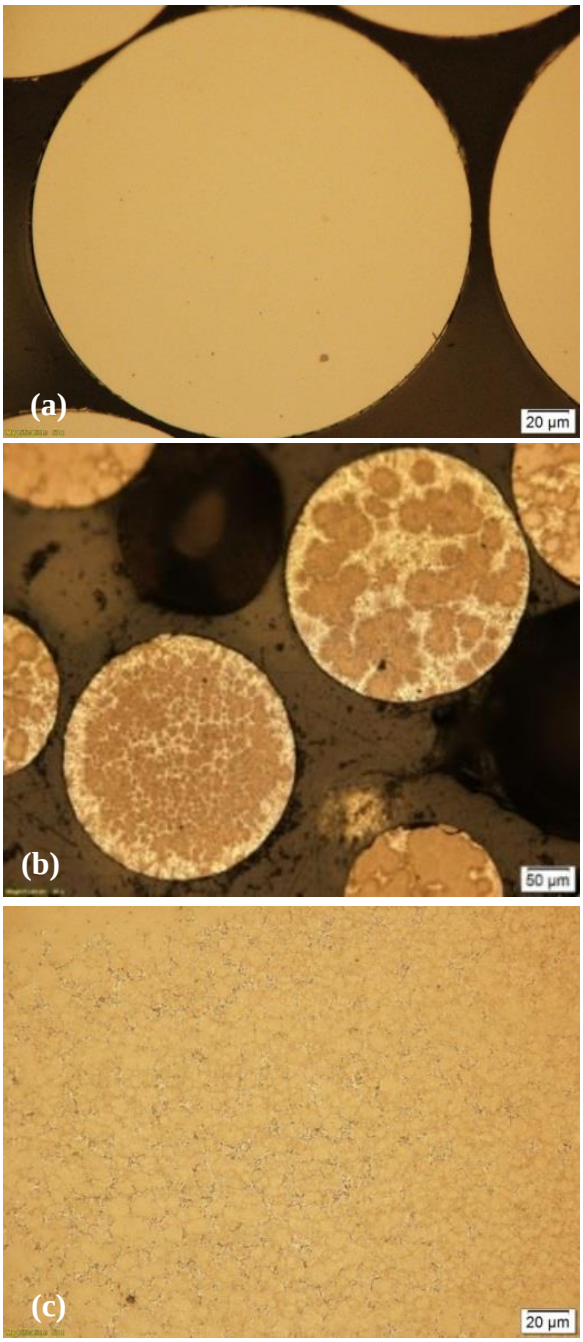

Figure 5: *Optical micrographs of (a) quasi- fully amorphous (212-250 µm), (b) partially amorphous (250-300 µm) and (c) fully crystalline (355-425 µm) IA powders*

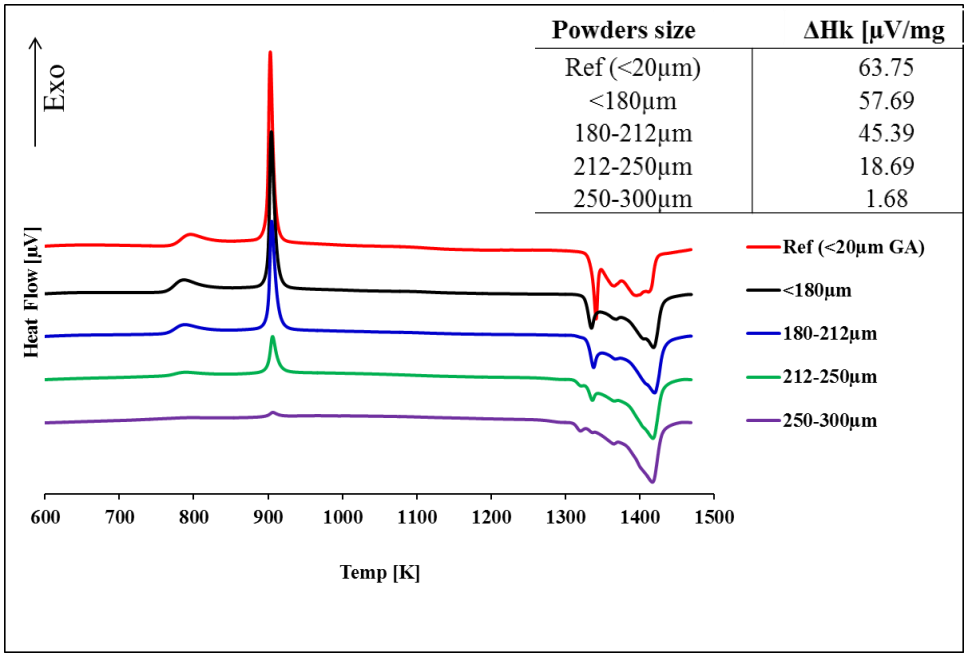

Figure 6: *DSC heating curves of the investigated powders, a tabulation of the enthalpy of recrystallization corresponding to each size range is shown at the top right corner of the figure. Experimental condition: A heating rate of 15K.min^{-1} from room temperature*

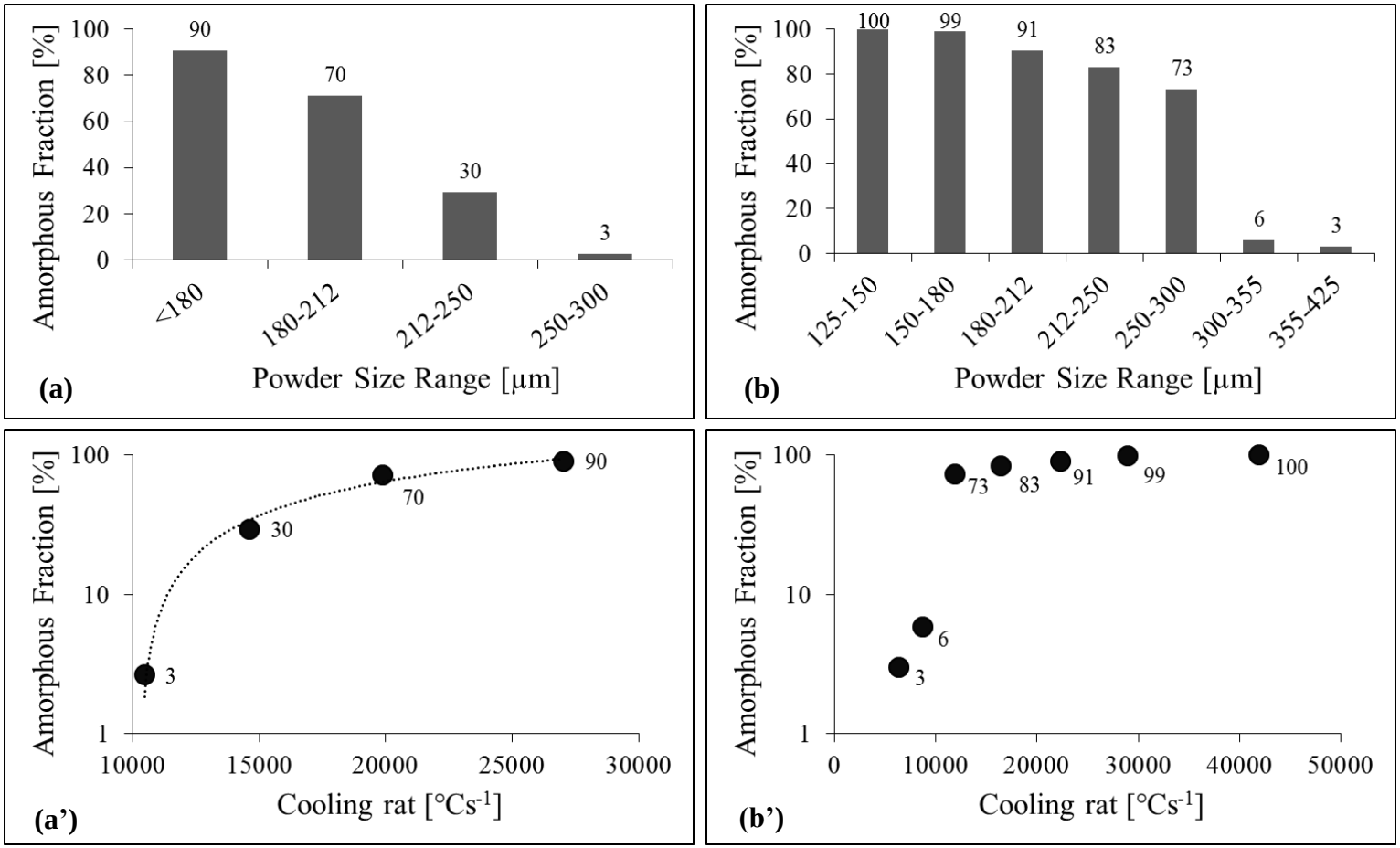

Figure 7: *Amorphous fraction variation respectively with powder size range and cooling rate (a&a') run#1, (b&b') run#2.*

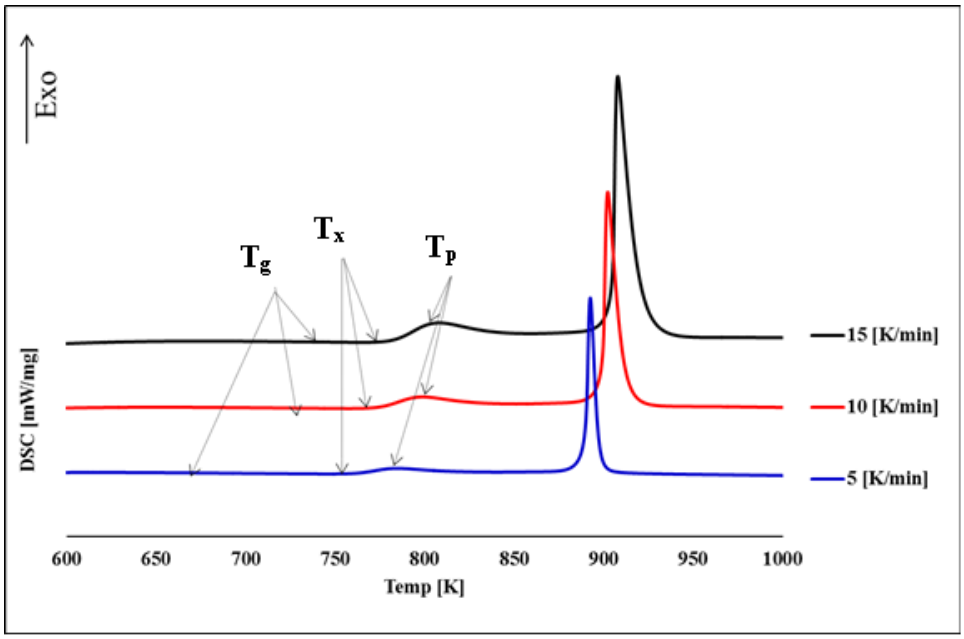

Figure 8: *DSC heating curves of the GA reference powders at three different heating rates from room temperature to 1470K under argon atmosphere*

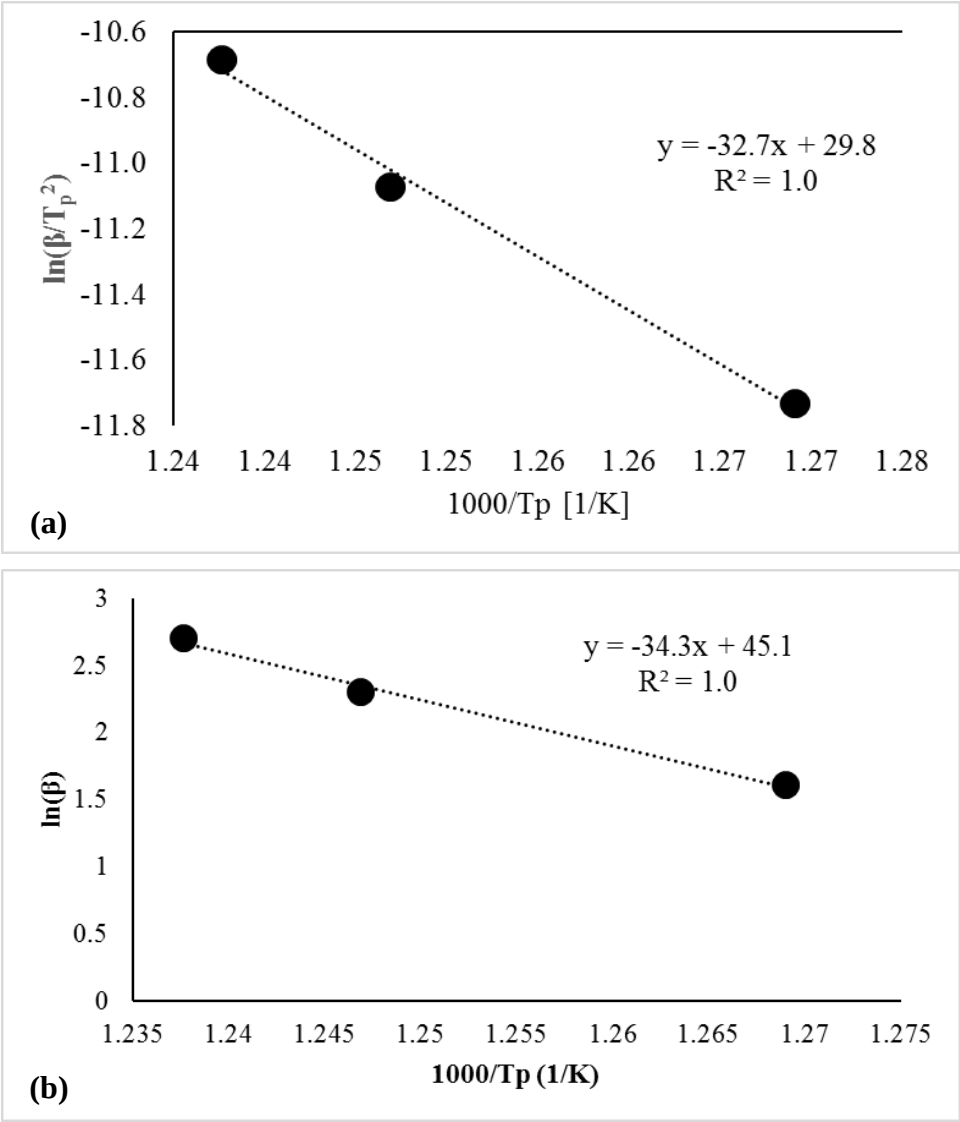

Figure 9*: The peak temperature of the first crystallization event (T_p) as a function of heating rate (β) following two models (a) Kissinger model (b) Ozawa model*

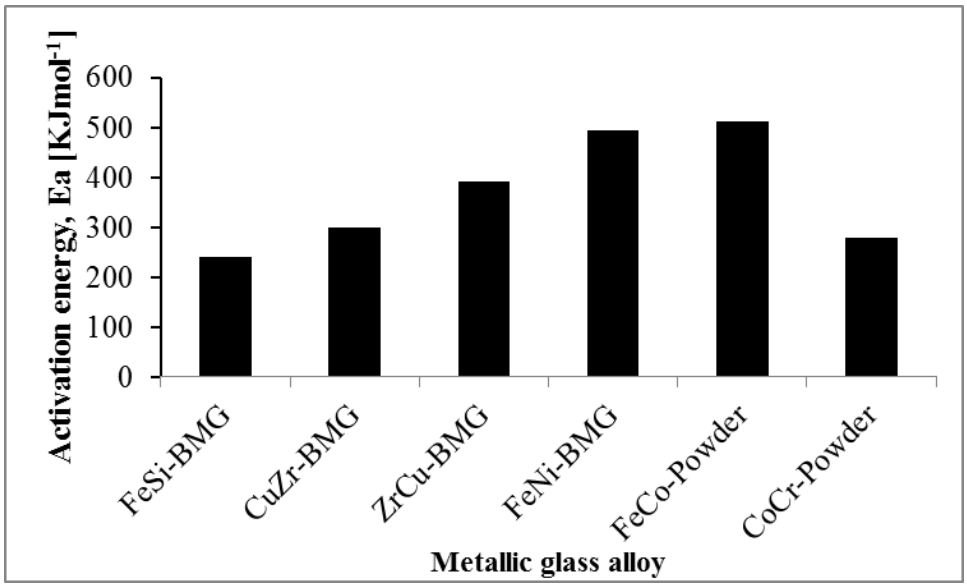

Figure 10: *Comparison of activation energies determined by the Kissinger and Ozawa models for different BMGs.*

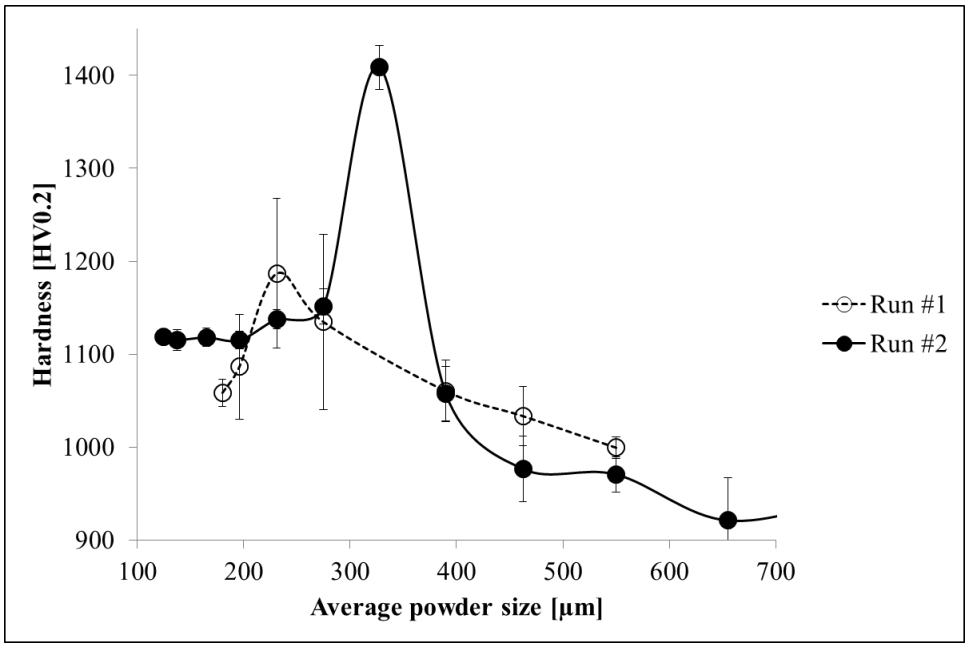

Figure 11: *Variation of average micro-hardness with average powder size. Test conditions: 200 gf test force and 5 sec holding time, 2 random indentations over surface of 10 powders*

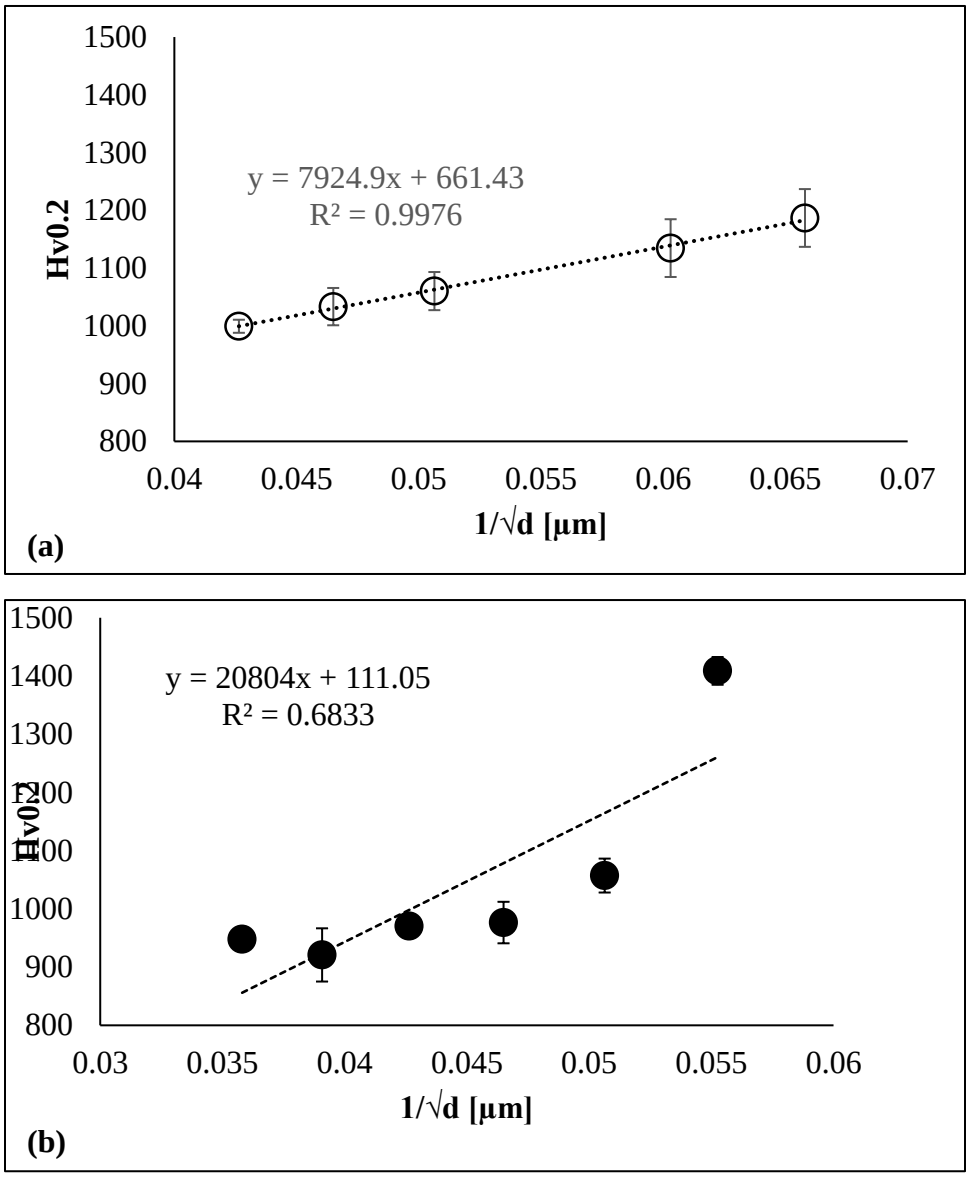

Figure 12: *Variation of average micro-hardness with the inverse square root of the average powder size, (a) run#1;(b) run#2. Test conditions: 200 gf test force and 5 sec holding time, 2 random indentations over surface of 10 powders*

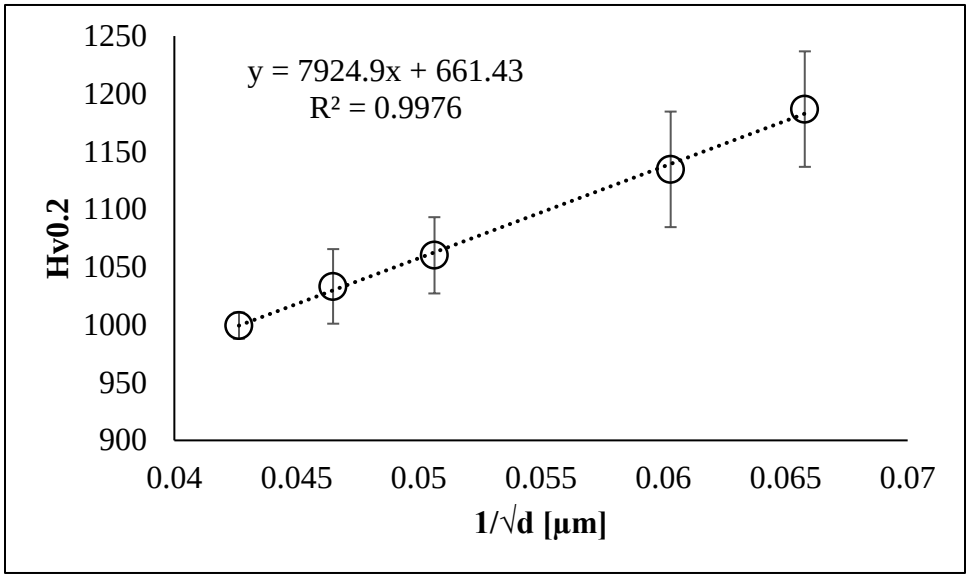
y = 7924.9x + 661.43
R² = 0.9976
Hv0.2
1250
1200
1150
1100
1050
1000
950
900
0.04
0.045
0.05
0.055
0.06
0.065
0.07
1/√d [µm]

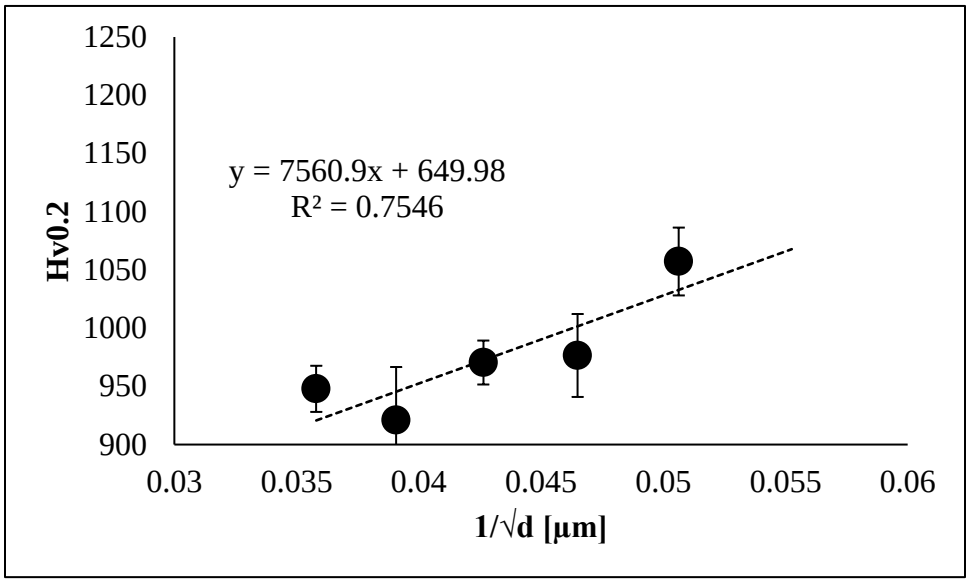
y = 7560.9x + 649.98
R² = 0.7546
Hv0.2
1250
1200
1150
1100
1050
1000
950
900
0.03
0.035
0.04
0.045
0.05
0.055
0.06
1/√d [µm]